





Cite this: DOI: 10.1039/c7cc08373d

New approaches to the lithiation kinetics in reaction-limited battery electrodes through electrochemical impedance spectroscopy

Nuria Vicente,^a Marta Haro ^b and Germà Garcia-Belmonte ^{*a}

Electrochemical impedance spectroscopy is a widely employed technique probing kinetic limitations in the charging of battery electrodes. Hindrance mechanisms locate at the interfaces between the active material and the electrolyte, and in the bulk of the reacting compound. Rate-limiting mechanisms are viewed as resistive circuit elements and can be extracted using standard impedance analyzers. Classical impedance models consider charge transport, mainly ion diffusion as slower carrier, as the principal kinetic limitation impeding full electrode charging. This is indeed the case for many technologically relevant battery compounds. In other instances, instead of being diffusion-limited, electrodes may undergo charging limitation caused by the kinetics of the reduction reaction itself. Specific impedance models for reaction-limited mechanisms are summarized here and proved for relevant electrode compounds, in particular for conversion or alloying electrodes in which Li⁺ intake produces a full rearrangement of the lattice structure with significant atomic displacement.

Received 31st October 2017,
Accepted 19th December 2017

DOI: 10.1039/c7cc08373d

rsc.li/chemcomm

^aInstitute of Advanced Materials (INAM), Universitat Jaume I, ES-12006 Castelló, Spain. E-mail: garciag@uji.es

^bOkinawa Institute of Science and Technology (OIST) Graduate University, 1919-1 Tancha, Onna-son, Okinawa 904-0495, Japan

Introduction

Electrochemical impedance spectroscopy (EIS) has been widely employed for decades as a standard characterization tool of battery electrodes.^{1–4} It consists of application of a small perturbation (usually a sinusoidal voltage) that slightly displaces the charge state of the electrode from a given steady state.



Nuria Vicente

Nuria Vicente is currently a PhD student in Sciences at Universitat Jaume I (Castelló), Spain. She received a Master's degree in Applied Physics from Universitat Jaume I in 2014. From 2013, she is a member of the Institute of Advanced Materials, where she develops research activity on new perovskite-based materials for storage energy and analysis of electrode kinetics using electrochemical impedance spectroscopy under the supervision of Prof. Germà Garcia-Belmonte.



Marta Haro

Marta Haro (PhD in Physical Chemistry, Universidad de Zaragoza, Spain, 2007) is a staff scientist at Okinawa Institute of Science and Technology (Japan). Prior to joining OIST, she worked as postdoctoral researcher in the Photovoltaic and Optoelectronic Devices group at Universitat Jaume I (Spain), in Adsorption and Environmental Protection on Porous Solids at Instituto Nacional de Carbon (Spain), and in Organophotonics group at University of Hull (UK). Her research interest is focused on the development of electrodes and their electrochemical and photoelectrochemical analysis for energy storage in Li-ion batteries, and other applications such as solar fuel generation from water splitting and photodegradation processes in water treatment.

The perturbation (10–20 mV) explores different time scales, usually in the frequency range of 1 MHz down to 1 mHz. This small deviation induces changes in transport and charging mechanisms involving ionic species (mainly the Li-ion in our case) of different time scales, response times or frequencies. As a consequence, EIS allows exploring the charging kinetics in battery electrodes using a non-destructive and easy-to-use experimental technique incorporated in commonly employed electrochemical testing systems. EIS is complementary to other well-established procedures such as the analysis of galvanostatic charge/discharge curves at different current intensities to determine the electrode rate capability and power response. In combination with structural techniques, EIS makes accessible the connection between particular electrochemical mechanisms and electrode morphology and constituents. This is the key point as to why EIS is a testing tool of absolute necessity in any electrochemical laboratory for diagnostic purposes.^{5–8}

The analysis of EIS spectra $Z(\omega)$, with ω being the angular frequency of the perturbation, is usually accomplished by fitting a proposed equivalent circuit to the data collected by the impedance analyzer. Elaboration of equivalent circuits able to capture the essential electrochemical mechanisms involved in the electrode response needs theoretical knowledge about capacitive (charging) and resistive (hindrance) processes occurring at the electrode.² These processes can be located at the interfaces between the active material and the electrolyte, and in the bulk of the reacting compound. Limitations to electrode charging stem from interface charge transfer mechanisms, as well as inner processes of the host. Rate-limiting mechanisms directly point to resistive circuit elements, which can be straightforwardly identified in the impedance plots in the complex plane ($Z'' - Z'$) for data visualization.⁹ Therefore, one can expect

resistances accounting for both interfacial and material bulk hindrance processes. Classical impedance models highlighted charge transport, mainly ion diffusion as slower carrier, as the principal limitation impeding full electrode charging.¹⁰ It is restriction to ion motion that delays full electrode reduction reaction and limits rate capability. This is so in many technologically relevant battery compounds.^{11,12} However, one cannot discard other origins for the delay in full charging. Instead of being diffusion-limited, electrodes may undergo charging limitation caused by the kinetics of the reduction reaction itself. In these cases, we can think about reaction-originated charging limitation. This mechanism should be characterized by a corresponding resistive element similar to that encountered for diffusion-limited electrodes. Because this is a much less explored process, the kinetics of reaction limitation, not related to the charge transport, will be addressed in this Feature Article.

The work is organized starting from relating resistive and capacitive circuit elements to the known electrochemical processes occurring in the electrode. Elementary circuit elements are then combined to provide full equivalent circuits mostly used for analyzing the kinetics mechanisms in battery compounds. Here, we give a brief summary of diffusion models and introduce the electrical representation for reaction-limited electrode analysis. This is accomplished by comparing the expected impedance spectra for the two cases, diffusion- and reaction-limited, signaling similarities and differences. After this brief outline about useful circuit models, the response of several electrode compounds is shown in the light of the impedance modeling. Both cathode and anode electrodes (LiFePO_4 , $\text{Li}[\text{Ni}_y\text{Co}_z\text{Mn}_{1-y-z}]\text{O}_2$, and TiO_2) are addressed indicating the potential use of the reaction models in a phenomenological way. These models are fully justified in the case of conversion and alloying electrodes for which a complete rearrangement of the material structure is expected. Here, the analysis is focused on several electrode materials with different morphologies (FeOOH , ZnFe_2O_4 and Si/Ge). To spread out the use of the impedance technique, we also present recent results and equivalent circuit interpretation of the impedance response of Li-O_2 electrodes. This Feature Article makes up an accessible summary of the application of electrochemical impedance spectroscopy to the study of the kinetics of battery electrode charging, stressing those cases limited by reaction-originated mechanisms.

Background: elementary circuit elements

Before summarizing the main impedance models and the most commonly used equivalent circuits of application in the battery analysis, it is interesting to point out some general features of the elementary circuit elements. Detailed information and theoretical background can be easily found in books for specialists,¹³ so our approach will be merely descriptive. Because battery electrodes are immersed in electrolytes containing a lithium reservoir, impedance measurement entails perturbation of processes at the electrode/electrolyte interface, in addition to those occurring within the electrode bulk material. When impedance spectra are analyzed, mechanisms at the outer interfaces



Germà Garcia-Belmonte

Germà Garcia-Belmonte joined the Universitat Jaume I de Castelló in 1992 and currently works as a Full Professor of Applied Physics (since 2010) at the Institute of Advanced Materials (INAM) which develops research activities on materials, nanostructures and devices for production and efficient use of clean energies. He studied intercalation processes in oxides and polymer films by impedance methods. He also conducted research in various areas within

the field of Organic Electronics and photovoltaics such as electronic mechanisms in organic light-emitting diodes, organic photovoltaics, and plastic and thin-film solar cells. He is currently active in the topic of perovskite-based solar cells. He is also interested in the electrochemical kinetics of electrodes for batteries. Device physics using impedance spectroscopy (including modeling and measuring) is his main subject.

(electrode/electrolyte) usually involve both capacitive and resistive processes.¹⁴ One of them is the ability of the interface to accumulate ionic species in the vicinity of the surface. The applied voltage modulates the amount of ions so as to produce a net capacitance classically known as the double-layer capacitance C_{dl} , because the interface charging occurs similarly to an electrical capacitor. The double-layer capacitance is a function of the dielectric properties of the interface. If an effective permittivity is defined for the contacting materials near the interface, the double-layer capacitance (per unit interface area) can be simply expressed as

$$C_{dl} = \frac{\varepsilon\varepsilon_0}{d} \quad (1)$$

Here ε accounts for the effective dielectric constant, ε_0 is the vacuum permittivity, and d represents the effective charge separation. Ions pile up at the interface producing thin space charge layers with net separation in the range of 1–10 Å. Using eqn (1), these distances imply double-layer capacitance values of the order of $C_{dl} \approx 10\text{--}100 \mu\text{F cm}^{-2}$, depending on the permittivity. The obvious strategy to increase the value of the total double-layer capacitor is to increase the interface area by means of porous matrices that allow electrolyte penetration and the formation on an extended double layer. For high porosities using nanostructured matrices, C_{dl} can attain values of several orders of magnitude in excess of the capacitive level shown by planar electrodes.

Interchange of charge carriers between the two constituents of the interface, usually labeled as a charge transfer mechanism, entails the injection/extraction of electronic carriers to/from the electrode material or the insertion/release of ionic species. The ionic (or electronic) charge transfer process occurs by surpassing an interfacial potential barrier, thereby governed by the energetic properties of the interface at a given charging state. Any barrier crossing involving charge carriers is accompanied by an energy loss, which in electrical terms is always modeled by means of resistive elements. This is why C_{dl} parallels a current-related circuit element usually known as charge transfer resistance R_{ct} . It is then a measurement of the interface permeability to the passage of charge. R_{ct} exhibits a dependence on the voltage related to the charge state of the electrode, usually with smaller values for lithiated electrodes. In some specific conditions R_{ct} is indeed the rate-limiting process, particularly when the electrode is highly charged and the inner ionic movement is fast enough. In many other cases, its contribution is comparable to the charging hindrance produced by solid state diffusion/reaction mechanisms inside the electrode material. The combination of C_{dl} and R_{ct} corresponds to the characteristic frequency commonly observed in impedance spectra as $\omega_{dl} = 1/R_{ct}C_{dl}$. In practical terms the double-layer characteristic frequency is situated at $\omega_{dl}/2\pi < 1 \text{ kHz}$, because it is usually observed that $R_{ct} < 1 \text{ k}\Omega \text{ cm}^2$. This means that establishment of the polarization state at the interface takes place in times of the order of ms in many practical cases.

Apart from processes occurring at the interfaces, independently of its porous or planar morphology, there is a set of

circuit elements connected to the electrochemical response of the electrode bulk to the variation in the applied potential. The fundamental element accounts for the charging ability of any battery electrode, and it is represented by a capacitive mechanism labeled as chemical capacitance C_{μ} .^{15,16} It is defined as the ratio between the variation in electrode charge state produced by a change in the electrode potential V . Here the electrode potential is assimilated to the chemical potential of Li^+ in the electrode μ , with respect to the chemical potential of the reference μ_{ref} (usually a Li metal film) as $V = -(\mu - \mu_{\text{ref}})/e$, with e being the positive elementary charge. The actual concentration of Li-ions in the electrode bulk depends on the total concentration N and the molar fraction in a given lithiated state x as $n = Nx$. In a battery electrode the ion chemical potential varies as a function of the amount of inserted charge $\mu(x)$, and this yields the steady-state charge–discharge curves. The chemical capacitance (per unit volume) can be then readily expressed as¹³

$$C_{\mu} = eN \frac{dx}{dV} \quad (2)$$

In eqn (2), C_{μ} has units of F cm^{-3} . Using the density of the active material, one can express it in units of F g^{-1} . The chemical capacitance is obviously related to the derivative of the discharge curve $-dQ/dV$ when very low charging rates are employed (quasi-equilibrium charging). We note here that C_{μ} and C_{dl} are essentially different. The chemical capacitance measures the response to the variations in the chemical potential, while the double-layer capacitance is of dielectric nature, that is, it depends on the changes of the electrical field at the interface. As explained previously, electrochemical impedance experiments try to capture the electrical response to the perturbation of an electrode steady state. By definition, eqn (2) gives information on the electrode low-frequency (long time) limit, which is ideally completely capacitive. In the highly lithiated state, battery electrodes always exhibit chemical capacitances in the range of $0.1\text{--}1 \text{ F cm}^{-2}$, taking into account the effective electrode thickness, in such a way that $C_{\mu} \gg C_{dl}$.

Before the electrode attains the steady state, several rate-limiting mechanisms may contribute to the polarization resistance hindering or delaying the charging. The transport of Li-ions inside the solid state bulk of the active material entails the crossing of local potential barriers between lattice sites. Concomitantly, ion transport is accompanied by energy loss, which in turn is electrically viewed as a resistance. This is the microscopic origin of the resistive mechanism behind the ion diffusion in the electrode material, which is called diffusion resistance R_d .¹⁷ The driving force for Li^+ transport relates to the ion chemical potential gradient $\Delta\mu$ between adjacent sites. The combination of R_d and C_{μ} (diffusion and charging) yields the well-known diffusion impedance models as later addressed.

Diffusion resistance is not the only hindrance process for electrode charging. For intercalation electrodes, the incorporation of ionic species does not excessively distort the lattice (topotactic intercalation). This implies that the reduction

reaction itself is energetically favorable involving minor energy losses. In contrast, for conversion or alloying electrodes Li^+ intake produces a full rearrangement of the host lattice structure with significant atomic displacement.¹⁸ In these last cases, the reaction itself, involving restructuring, kinetically governs the charging process. Again, the reaction can be assimilated to an energy barrier surpass and represented by a resistive element, called reaction resistance R_r . This resistance gathers information on the overall energy losses involved in the solid-state reaction, including atomic rearrangement. The rate-limiting mechanism can be determined by either R_d or R_r depending on the kinetically slowest process. The combination of R_r and C_μ (reaction and charging) also yields distinctive impedance responses. Either diffusion-limited or reaction-limited, these last circuit elements operate within the low-frequency range of the measuring frequency window (Hz–mHz).

Finally, there are in some cases minor contributions in the high-frequency range (> 1 kHz) originated from the response of external layers. The solid electrolyte interface is commonly formed after cycling and introduces RC subcircuits connected in series to the rest of the electrode equivalent circuit. The capacitive values are often in the range of nF– μF , because they are originated by dielectric responses of thicker films compared to the double-layer thickness.

Basic impedance models

The previously introduced circuit elements combine to make up the equivalent circuits used for fitting and data analysis of impedance responses in battery electrodes. A useful starting point is recalling the simplest Randles' circuit that gathers the main response mechanisms and simplifies hindrance processes.¹⁹ It is shown in the equivalent circuit of Fig. 1a along with its corresponding impedance plot in the $Z'' - Z'$ complex plane. At high frequencies, R_{ct} and ω_{dl} can be directly read (from the real axis intercept and the maximum in Z'' , respectively) and C_{dl} easily derived. The low-frequency response is dominated by the chemical capacitance because, in this simple circuit, all possible rate-limiting mechanisms in the bulk material are discarded when solid-state diffusion restrictions disappear. It is noted here that battery electrodes rarely exhibit "ideal" capacitors accounting for either interfacial or bulk mechanisms. Instead, capacitance generalizations such as the well-known constant phase element (CPE) are used with impedance¹⁷

$$Z_{\text{CPE}} = \frac{1}{Q(i\omega)^n} \quad (3)$$

Here $i = \sqrt{-1}$, ω is the angular frequency of the perturbation, and Q assimilates to the capacitance. CPE circuit elements should be considered as phenomenological descriptions of complex responses, in many cases connected to energetic or structural disorder. This element approaches pure capacitive responses in the case of $n = 1$ with $Z_C = 1/i\omega C$. For $0.8 \leq n \leq 1$ one can consider that the impedance maintains the capacitive character. As observed in Fig. 1b, CPE elements distort the high-frequency arc and yield inclined low-frequency responses.

The next step is the inclusion of solid-state diffusion processes hindering the charging (capacitive) response of the electrode. Ion diffusion is an intricate mechanism that involves the transport of electronic carriers to ensure the material electro-neutrality. Fortunately, electronic movement is usually faster than the ionic one, at least for most of the battery electrodes of technological interest. This fact allows considering the diffusion of the ionic species (the slowest charge carrier) as the rate-limiting factor for electrode charging. In the simplest planar electrode structure, the model accounting for this mechanism is the so-called spatially restricted diffusion model, which exhibits the so-called diffusion impedance, Z_D in Fig. 1c.²⁰ Diffusion impedances undergo a pattern change at a certain characteristic frequency ω_d at which a transition between a Warburg- and a capacitive-like behavior is observed.^{21,22} The frequency ω_d is located near the elbow of the impedance plot in Fig. 1c, and relates to the ion chemical diffusion coefficient D_μ as

$$\omega_d = \frac{D_\mu}{L^2} \quad (4)$$

Here L corresponds to the diffusion length and is related to the thickness of the electrode. The finite-length diffusion element is given by

$$Z_D = R_d \left(\frac{i\omega}{\omega_d} \right)^{-\gamma/2} \coth \left[\left(\frac{i\omega}{\omega_d} \right)^{-\gamma/2} \right] \quad (5)$$

R_d is the resistance associated with the ionic diffusion, and γ relates to the deviation from the ideal spatially restricted diffusion impedance ($\gamma = 1$) in Fig. 1c. The anomalous diffusion mechanism ($\gamma < 1$) in Fig. 1d is expected to occur in a multi-phasic matrix.²³ Diffusion of ions gives rise to distinctive impedance patterns characterized by Warburg-like responses as $Z \propto (i\omega)^{-\gamma/2}$ at intermediate frequencies. At lower frequencies the electrode charging produces the capacitive response through the chemical capacitance C_μ . It is related to the characteristic diffusion frequency in eqn (4) as

$$\omega_d = \frac{1}{R_d C_\mu} \quad (6)$$

The equivalent circuit of Fig. 1c and d includes the diffusion impedance model of eqn (5) as an independent element Z_D whose response varies in frequency in such a way that it exhibits two different frequency limits. Z_D is of general application for intercalation electrodes (topotactic insertion) in which it is well-established that the ion diffusion is the rate-limiting mechanism for electrode charging.

A different impedance model results from considering that the charging process is limited by the solid-state reaction itself. That is to say that the rate-limiting mechanism is governed by microscopic processes occurring for the electrode material reduction different from the Li^+ transport. The formulation of this kind of impedance model has deserved much less attention than the diffusion counterparts and only a few works have addressed the issue, particularly for conversion and alloying electrodes.^{24,25} Here the reduction reaction involves a large morphological restructuring, in many cases producing

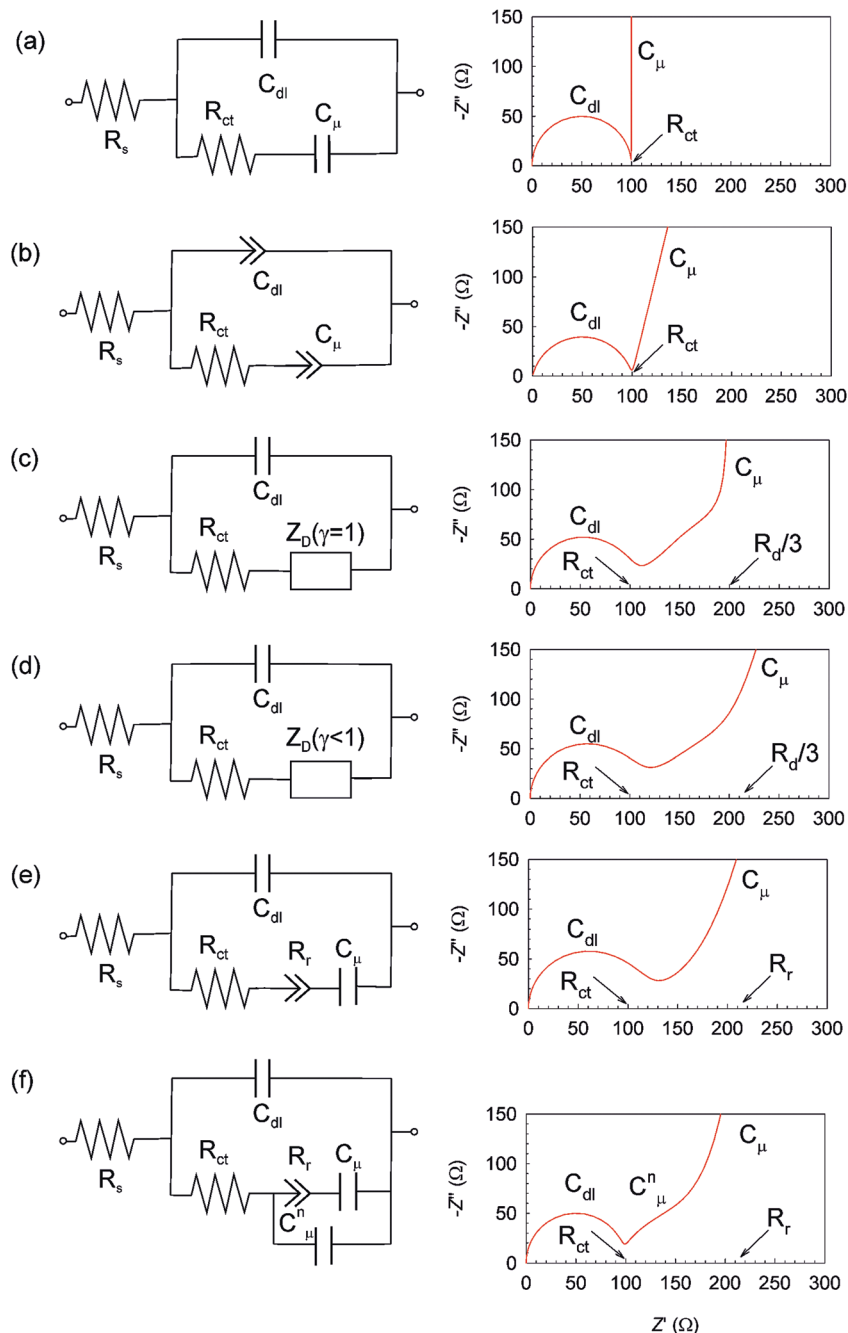


Fig. 1 Equivalent circuits and their corresponding impedance plot ($Z'' - Z'$ complex plane) for different battery electrode mechanisms. R_s accounts for the solution resistance. (a) Ideal Randle's circuit without any solid-state charging limitation. (b) After incorporating constant-phase elements (CPE) in substitution of pure capacitances. (c) Ideal spatially limited diffusion model Z_D with disorder parameter $\gamma = 1$. (d) Anomalous spatially limited diffusion model Z_D with disorder parameter $\gamma < 1$. (e) Reaction-limited model including the generalization of reaction resistance. In all the plots: $C_{dl} = 1 \mu\text{F}$, $C_{\mu} = 1 \text{mF}$ and $R_{ct} = 100 \Omega$. (b) $n = 0.85$ for both capacitances. (c) $R_d = 300 \Omega$ and $\gamma = 1$. (d) $R_d = 300 \Omega$ and $\gamma = 0.85$. (e) R_r , calculated using $Q = 0.005 \Omega^{-1} (\text{is})^{-n}$ and $n = 0.2$ in eqn (3). (f) Including $C_{\mu}^n = 100 \mu\text{F}$.

amorphous materials. As previously explained, one can gather all energy-loss processes occurring during the conversion reaction into an effective resistive element R_r . It is known that reactions occur in an energetically and structurally complex environment that forces the spread of the reaction characteristic times (or frequencies). The characteristic time distribution caused by the inherent disorder can be incorporated into a

generalization of the reaction resistance similarly to that used for generalizing capacitances. The CPE circuit element in eqn (3) with an exponent $n = 0$ can be viewed as a pure resistor. Therefore, a Z_{CPE} with $0 \leq n \leq 0.3$ has been proposed for modeling the hindrance in conversion electrode charging.²⁵ Hence, R_r connected in series with C_{μ} conveys the intuitive idea that the restriction for electrode charging takes place in the

same current branch. This is specified in the impedance model of Fig. 1e which gives rise to an impedance plot exhibiting a slow transition to the low-frequency capacitive limit. Some special cases exhibit a multistep conversion reaction, with the overall process being modeled by several $R_r C_\mu$ branches.²⁵

Similarly to the characteristic diffusion frequency in eqn (6), one can define the characteristic reaction frequency ω_r using the CPE expression in eqn (3). ω_r informs on the time scale of the conversion reaction as

$$\omega_r = \left(\frac{Q}{C_\mu} \right)^{\frac{1}{1-n}} \quad (7)$$

The conversion frequency in eqn (7) allows defining an effective conversion resistance accounting for the overall resistive contribution of the reaction from

$$\omega_r = \frac{1}{R_r C_\mu} \quad (8)$$

It is stressed that whether diffusion- or reaction-limited the electrode kinetics can be represented by a well-defined characteristic frequency in eqn (6) and (8). In some relevant cases the distinction between both kinds of impedance models is not straightforward and mainly depends on the analysis of additional tests (electrode thickness or morphology variation, changes in electrolyte composition, *etc.*) that might assist in the model selection. In other cases, both diffusion and restructuring contribute to the kinetic limitation, with the separation of their individual influences being unachievable in terms of well-distinguished characteristic frequencies. Here, the estimation of a response frequency and effective hindrance resistance can be made using the model in Fig. 1e, which suffices as a phenomenological approach for many practical purposes.

In some experiments, intermediate-frequency distortions appear involving an arc just before the low-frequency capacitive behavior governed by C_μ . Previous analyses connected these trends to distributions of diffusion lengths,²⁶ or electronic transport limitations.²⁷ It can be also linked with an extra chemical capacitance C_μ^n accounting for the presence of “free” Li^+ ions in the storage material. These ions occupy sites in the host lattice that do not belong to kinetically stable charging locations, which gives rise to the defined C_μ . A theoretical model was previously introduced.²⁴ Fig. 1f shows the proposed equivalent circuit, including C_μ^n , along with an example of the impedance plot.

So far we have been dealing with the impedance response of compact electrodes. If the electrolyte penetrates the electrode and wets the active particles the effective diffusion length in the solid-state may be significantly reduced, $L_{\text{eff}} \ll L$, in comparison to the electrode thickness giving rise to large overestimations in D_μ . The so-called porous impedance model allows addressing these last cases.^{26–28} Hence, it is a matter of experimental checking to discern if $L_{\text{eff}} \approx L$, in such a way that the finite-length diffusion mechanism in eqn (4) can be consistently used to determine D_μ . The porous models rely on the formation of an extended double-layer in the vicinity of the

active particles inside the electrode matrix. It is expected then that larger values for C_{dl} are obtained. It should be also noted that in some instances, the sole analysis of the impedance response is not often enough to decide about the compact or porous character of the electrode and additional tests are needed here to make a distinction.

In practical measuring terms, the impedance response is affected by several parameters that should be controlled during the measurement. Applied dc voltage is established by the impedance analyzer in such a way that the electrode is probed at a given state of charge. As expected, and illustrated later, the impedance response is highly dependent on the potential value.^{29,30} All the impedance elements, either interfacial- or bulk-related, may evolve with potential, for instance electronic and ionic transport resistances,³¹ and also capacitive elements.³² Another influential factor is temperature. The effects of temperature and thermal management on capacity/power fade, thermal runaway, and pack electrical imbalance and the performance of lithium-ion cells at cold temperatures are indeed central technology issues.³³ It is well known that carrier diffusion is a thermally activated process, so electronic transport through contacting layers and also charge transfer resistance can be investigated by probing the electrode at several temperatures using EIS. This approach informs on the activation energy of the processes.³⁴ By monitoring with EIS the resistive contributions to the total electrode resistance with temperature, it was observed that both the power (operating voltage) and energy (delivered capacity) are substantially reduced at low temperature.³⁵ Hence temperature can be used as a probing parameter to identify specific mechanisms through impedance variations, exhibiting in some cases additional features connected to the solid electrolyte interphase.³⁶ Finally, battery electrodes evolve with cycling and so does impedance response. Capacity fading and aging upon cycling can be alternatively explored by monitoring the low-frequency impedance change with cycle number. In the same way, diffusion coefficient reduction is accessible by programing impedance analyses at different cycles.^{37,38}

In the following, we address the electrochemical response of several electrode materials in the light of the previously described impedance models. Attention will be paid to the kinetics mechanisms to illustrate the use of the models, rather than detailing the charge/discharge profiling and the general performance of the electrode.

Cathodes: $\text{Li}[\text{Ni}_y\text{Co}_z\text{Mn}_{1-y-z}]\text{O}_2$ and LiFePO_4

To start with we discuss the impedance response of two kinds of actively studied cathode materials: the layered oxide $\text{Li}[\text{Ni}_{0.8}\text{Co}_{0.06}\text{Mn}_{0.14}]\text{O}_2$ ³⁹ and the olivine LiFePO_4 .⁴⁰ In the former the transition metal (TM) is linked directly to the O atom, while in the latter the TM is bonded to a polyanion. In consequence, the O in the TM oxides shows high nucleophilic character that can rapidly react with the electrophilic alkyl carbonate molecules of the liquid electrolyte and the acidic species formed from the decomposition of salt during the cycling of the battery. The presence of covalently bonded PO_4 units in the case of LiFePO_4 leads to good structural and chemical stability without

the liberation of oxygen. On the other hand, the different Li arrangement in both cathodes (interconnected interstitial sites in the layered oxide while Li and Fe cations are located in half of the octahedral sites in the case of the olivine) provides slower Li ion diffusion (σ_{Li}) in LiFePO₄ compared to Li[Ni_{0.8}Co_{0.06}Mn_{0.14}]O₂.⁴¹ Also, the electrical conductivity (σ_e) in the former is higher than in the latter. In consequence, LiFePO₄ shows low rate capability compared to Li[Ni_{0.8}Co_{0.06}Mn_{0.14}]O₂. These features are reflected in the parameters determined by experimental EIS measurements and analyzed with the equivalent circuit modeling.

For both cathodes, Li[Ni_{0.8}Co_{0.06}Mn_{0.14}]O₂ and LiFePO₄, the same equivalent circuit model can be applied, which corresponds to the kind drawn in Fig. 1f, with the additional inclusion of a high-frequency parallel $R_{sf}C_{sf}$ subcircuit. In this model, R_{sf} and C_{sf} yield an arc related to the resistance and capacity of the Li ions' rapid diffusion through the solid film (SF) formed at the cathode–electrolyte interface due to the decomposition reactions during lithiation–delithiation processes.^{39,40} The use of the model in Fig. 1f is adopted here as a phenomenological approach in the case of multiparticle electrodes even with the rate-limiting mechanism dominated by ion diffusion. It allows extracting the influence of hindrance processes and compare electrode performances.

In the case of Li[Ni_{0.8}Co_{0.06}Mn_{0.14}]O₂, the two subcircuits (interface- and bulk-originated) in Fig. 1f and the additional high-frequency contribution can be clearly identified in the EIS spectra, shown in Fig. 2a. The two arcs at high frequency are related to the interfacial processes (resistances assigned to the SF and charge transfer) and that at low frequencies are assigned to the chemical energy storage mechanism. In particular, Fig. 2a shows the EIS spectra registered at 3.9 V during the lithiation process of the cathodes of general formula Li[Ni_{0.8}Co_{0.06}Mn_{0.14}]O₂, but with different atomic distribution: conventional composition (CC) and two-sloped full concentration gradient (TSFCG).³⁹ The core in TSFCG particles is rich in Ni (cation responsible for high capacitance) while the concentration of Mn increases on the surface layer of composition Li[Ni_{0.64}Co_{0.06}Mn_{0.30}]O₂. Among the three TM, Ni is reported to enhance the nucleophilicity of the O, and is more surface reactive than the other two species (Co and Mn).⁴² Then, the lower concentration of Ni in the surface layer of TSFCG structure reduces the reactivity of the cathode with the electrolyte and, in consequence, the resistance related to the SF is one order of magnitude lower. The formation of SF affects the capacity fade; TSFCG shows capacity retention of ~90% after 100 cycles, while for CC it is ~78%.

EIS measurements also show that the main operating difference between CC and TSFCG electrodes is kinetic and not thermodynamic. This effect is clearly observed through the determination of C_{μ} from EIS, which theoretically corresponds to the differential charge change in the electrode upon voltage variation in the quasi-equilibrium state $-dQ/dV$, calculated from the measurements of the charge–discharge curve. C_{μ} values determined from the equivalent circuit model (Fig. 1f) and charge–discharge measurements are provided in Fig. 2b.

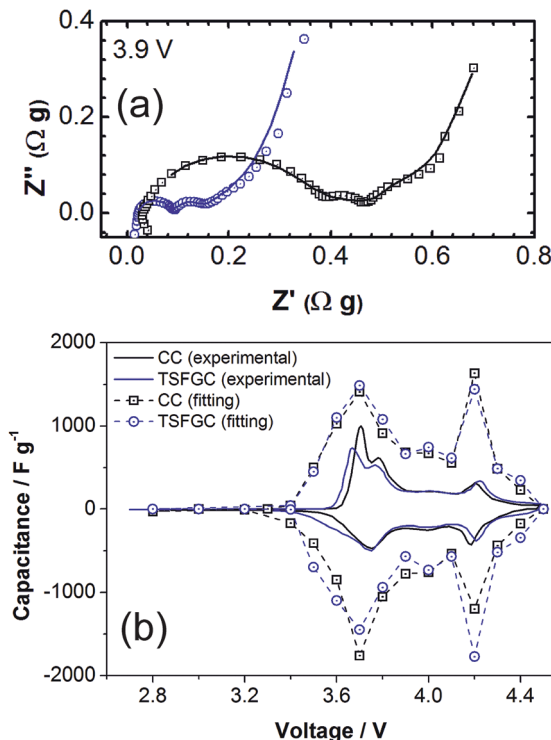


Fig. 2 (a) Impedance plots at 3.9 V during the lithiation process in TSFCG and CC positive electrodes. The experimental data are represented by points and the fitting with solid lines. (b) Chemical capacitance of the CC and TSFCG cathodes obtained from $-dQ/dV$ of the charge/discharge measurements at 0.1 C, and C_{μ} calculated from the EIS data. Reproduced (adapted) from ref. 39 with permission from the Royal Society of Chemistry.

From both methods, the capacitance shows the typical redox peaks associated with the overall reaction $Li_x(Ni_y^{2+}Co_z^{3+}Mn_{1-y-z}^{4+})O_2 \leftrightarrow (Ni_y^{2+}Co_z^{3+}Mn_{1-y-z}^{4+})O_2 + xLi^+ + xe^-$. The larger values extracted from EIS measurements in comparison to galvanostatic experiments are caused by the different experimental conditions: the former are extrapolated from the low-frequency limit (quasi steady-state) while the latter cannot be regarded as a true steady-state even at the low current rate of 0.1 C. More interesting is the fact that in dynamic measurements (charge–discharge and cyclic voltammetry measurements) the peak at 4.2 V (ascribed to either the Co oxidation state change or oxide phase transition) is lower than at 3.7 V (assigned to the change in the oxidation state of Ni).^{43,44} Meanwhile, C_{μ} values obtained from EIS are slightly higher for the peak registered at 4.2 V. This fact together with the similarity in C_{μ} values from EIS for both CC and TSFCG electrodes points out that the lithiation/delithiation processes are kinetically rather than thermodynamically inhibited in the studied cathodes.

While EIS measurements show the critical formation of SF films in Li[Ni_{0.8}Co_{0.06}Mn_{0.14}]O₂ cathodes, this detrimental film is not (or scarcely) formed in the family of LiFePO₄ positive electrodes. The low reactivity of LiFePO₄ cathodes with the electrolyte is observed in Fig. 3a, where the arc at high frequency related to the SF cannot be observed at all. In this case, EIS analysis shows two patterns: a flattened arc at high frequencies linked to the interface-related $R_{ct}C_{dl}$ subcircuit, and a capacitive behaviour

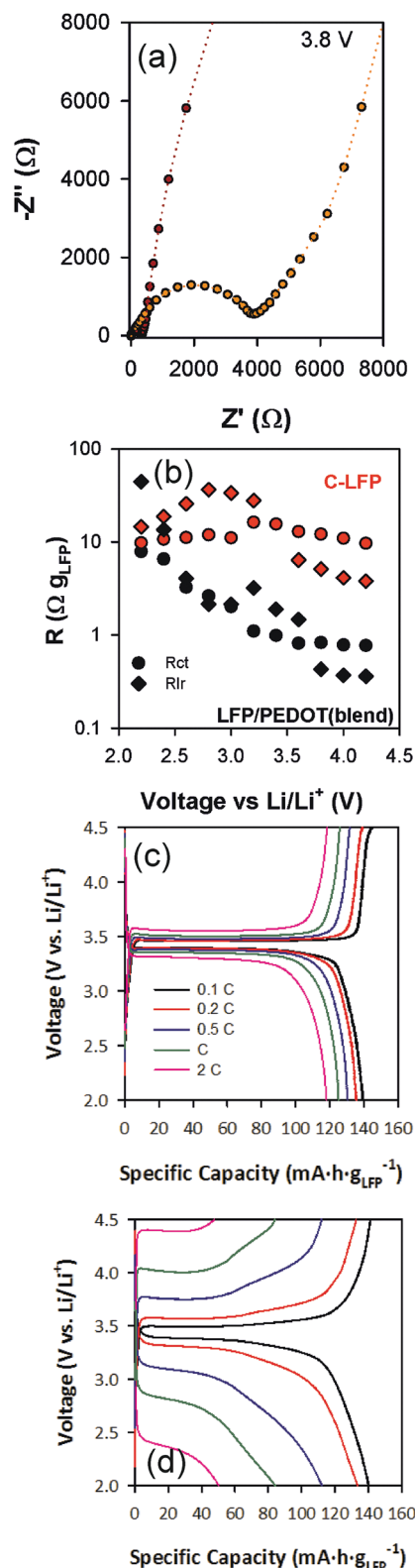


Fig. 3 (a) Impedance plots of measured (dots) and fitting results (lines) at 3.8 V of discharge for LFP/PEDOT(blend) (red dots) and C-LFP (yellow dots). (b) Fitting parameters in the discharge process for LFP/PEDOT(blend) (black symbols) and C-LFP (red symbols): R_{ct} is symbolized by circles and R_{lr} by rhombus. Charge–discharge curves at different rates for (c) LFP/PEDOT(blend) and (d) C-LFP. Reproduced (adapted) from ref. 40 with permission from Elsevier.

associated with the Li ion storage inside the cathode, manifested by C_{μ} .

Two different strategies to increase the Li ion diffusion and electronic conductivity of LiFePO_4 (LFP) were tested by introducing molecular wiring with carbon (C-LFP) and PEDOT:PSS (LFP/PEDOT(blend)).⁴⁰ The two resistances (R_{ct} and R_r) that hinder lithiation/delithiation processes in these cathodes can be estimated by means of the equivalent circuit model, shown in Fig. 1f. The estimated values for the lithiation process are shown in Fig. 3b, which shows that PEDOT:PSS reduces the charge transfer resistance more effectively than C, practically by one order of magnitude above 3.4 V.⁴⁵ Below this voltage, R_{ct} of the LFP/PEDOT(blend) electrode starts increasing, and at 2.2 V both cathodes show similar values. Also, lower R_r values are obtained for LFP/PEDOT(blend) than for C-LFP, indicating that the introduction of the electric molecular wiring also influences the lithiation reaction resistance of the phosphate matrix. In this regard, the use of PEDOT(blend) is an effective strategy to reduce the resistances that govern LFP lithiation/delithiation processes due to the high conductivity of both electrons and ions of the polymer,⁴⁶ and the good embedded structure of the LFP nanoparticles in the PEDOT matrix. This is reflected in the charge–discharge plots of LFP/PEDOT(blend) and C-LFP cathodes, Fig. 3c and d. At 0.1 C, both cathodes show similar capacity and low hysteresis, but with the increase of the charge–discharge rate, the hysteresis effect is more noticeable in the C-LFP cathode at the same time that the capacity decreases.

Anodes: MWCT@TiO₂ and MAPbBr₃

To improve the handicaps that materials for lithium ion battery (LIB) anodes present at high cycling rates, such as low Li^+ diffusion, scarce electron transport and high resistances at the electrode/electrolyte interfaces, new approaches and new materials are studied. Combining different materials allows creating composites with superior properties than the pristine counterparts. Multiwalled carbon nanotube and TiO_2 (MWCNT@TiO₂) composites as anodes led to improvement in the electronic transport offered by carbon, and to the reversibility of Li^+ ion insertion and mechanical stability provided by TiO_2 . Also, a specific capacity as high as 250 mA h g^{-1} was delivered, which is double that encountered for TiO_2 -based anodes.⁴⁷ Impedance analysis typically shows two patterns with distinguishable time constants associated to interfacial and charging mechanisms. As shown in Fig. 4, the composite (MWCNT@TiO₂) exhibits resistive components connected to the transport of Li^+ ions before reaching stable sites inside the active matrix.

In the case of the pure TiO_2 -electrode at high voltage, R_{ct} is so high that it does not allow detecting the other process within the measuring frequency range. According to Fig. 1f, the low-frequency part of the spectra conveys information on R_r (lithiation reaction) and C_{μ} (chemical capacitance). A summary of the parameters extracted from fitting, during charge and discharge in potentiostatic mode, is depicted in Fig. 5.

Firstly, the high-frequency elements R_{ct} and C_{dl} (Fig. 5a and b) exhibit rather voltage-independent values for electrodes comprising MWCNTs, with and without TiO_2 . Although at lower potentials

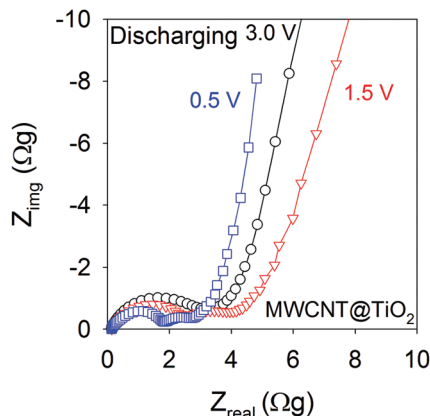


Fig. 4 Impedance response of MWCNT@TiO₂ electrodes at different discharge potentials. Reproduced (adapted) from ref. 47 with permission from Elsevier.

both TiO₂ and MWCNT@TiO₂ are able to insert Li⁺ ions with similar (diminished) hindrance, when the voltage increases over 1.5 V, a much larger charge transfer resistance is observed for pristine TiO₂ (~10 Ω g) compared to MWCNT@TiO₂, which keeps it at ~1 Ω g. It is known that R_{ct} is directly related to the electronic conductivity of the host material,⁴⁸ because conductive hosts facilitate the Li⁺ ion to overcome the potential barrier appearing at the electrolyte/semiconductor interface, in such a way that MWCNTs assist the Li⁺ ion incorporation into the TiO₂ matrix through the formation of Ti–C bonds.⁴⁷

The chemical capacitance C_{μ} in Fig. 5c exhibits well-defined peaks for both MWCNT@TiO₂ and TiO₂ electrodes in the lithiation-reaction voltage range, with comparable values around 250 F g⁻¹. The resistance accompanying the lithiation reaction R_r

also shows a similar behavior giving values of 1–3 Ω g (Fig. 5d). Differences of a factor of two are observed in R_r between MWCNT@TiO₂ and TiO₂ electrodes probably related to the strain in TiO₂ particles caused by the MWCNT/TiO₂ interface, which slightly modifies the lithiation reaction kinetics. Therefore, TiO₂ and MWCNT@TiO₂ exhibit comparable specific capacity, but the charge transfer resistance for the latter is reduced by a factor of 10, implying a key role of MWCNTs in favoring the interfacial Li⁺ ion intake from the electrolyte. This is the main mechanism that explains the superior rate capability (power performance) observed for MWCNT@TiO₂ in comparison to TiO₂ electrodes.

On the other hand, recently hybrid halide perovskites have been reported as promising charge-storage materials for lithium-ion battery anodes.^{49,50} These compounds have interesting electronic and photonic properties, and ionic migration allows for a variety of applications in electrochemical devices. The hybrid perovskite CH₃NH₃PbBr₃ has been utilized as an active material as anode, which behaves as a compact structure in which the dimensionality of Li⁺ transport is 3D. As the perovskite lithiation progresses, specific capacity values as high as 400 mA h g⁻¹ are reached (Fig. 6a), which implies a Li-ion concentration as high as 10²¹ cm⁻³, given perovskite densities approximately equal to 4.16 g cm⁻³. The host matrix becomes fully lithiated at potentials below 0.5 V vs. Li/Li⁺.⁴⁹ The chemical diffusion coefficient of lithium ions within the perovskite lattice exhibits values as high as $D_{\mu} \approx 10^{-7}$ cm² s⁻¹, which implies ionic conductivity within the range of 10⁻³ Ω⁻¹ for highly lithiated electrodes. The impedance plots (Fig. 6b) can be modeled by the equivalent circuit in Fig. 1d. The intermediate- and low-frequency impedance response exhibits clearly a diffusive-capacitive behavior that depends on the voltage (charging) state. Diffusion impedances

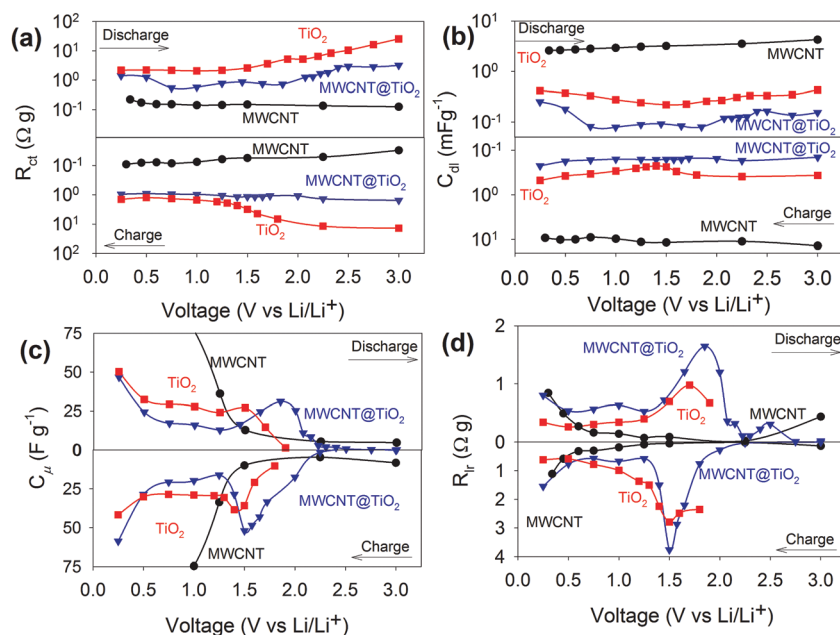


Fig. 5 Parameters derived from fitting of EIS data for TiO₂-based electrodes: (a) charge transfer resistance R_{ct} , (b) double layer capacitance C_{dl} , (c) chemical capacitance C_{μ} , and (d) lithiation-reaction resistance $R_r = R_r$. Reproduced (adapted) from ref. 47 with permission from Elsevier.

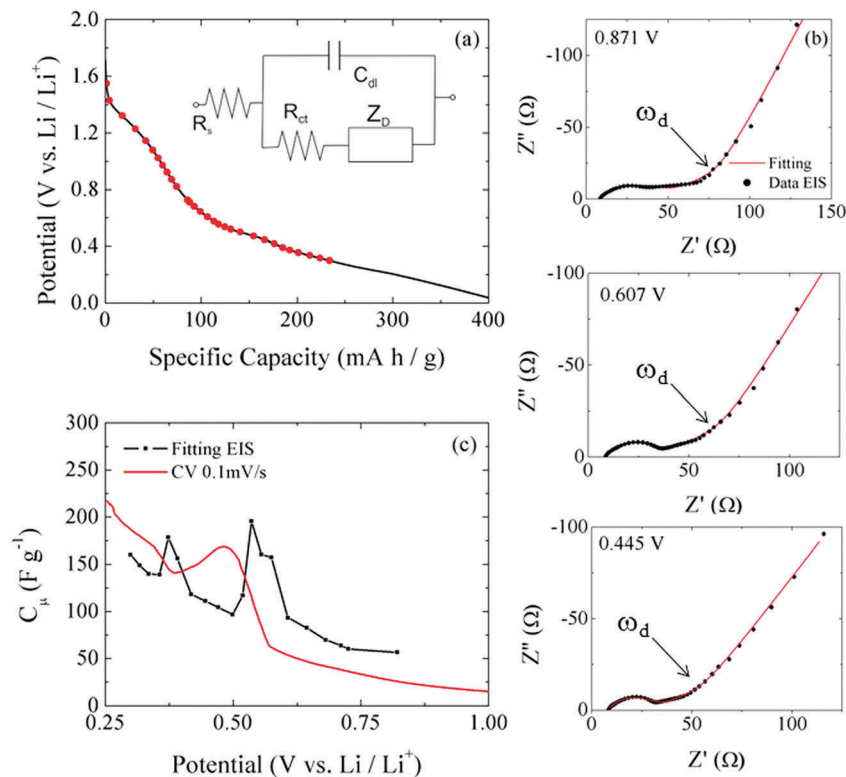


Fig. 6 (a) Selected potentials and charge state of the electrode lithiation process for *in situ* EIS analysis during the discharge process of $\text{CH}_3\text{NH}_3\text{PbBr}_3$ anodes. Inset: Equivalent circuit used Fig. 1d. (b) Impedance spectroscopy response at different steady-state voltages. The solid line corresponds to fits using the equivalent circuit. The diffusion response frequency ω_d is marked. (c) C_μ calculated from different data: EIS and cyclic voltammetry as $-dQ/dV$ plotted vs. potential during the discharge process. Reproduced from ref. 50 with permission from Wiley-VCH.

undergo a pattern change at a certain characteristic frequency ω_d (eqn (4) and (6)) at which a transition between a Warburg- and a capacitive-like behavior is observed. The superionic property of organohalide perovskites can be exploited in applications and devices in which fast ionic migration is an essential requirement.

Conversion and alloying anodes: FeOOH , ZnFe_2O_4 and Si/Ge

In this section, a review about the use of the impedance technique for analyzing conversion and alloying anodes is done. Three of the more promising alternatives to carbon anodes were characterized: conversion-reaction of amorphous iron oxyhydroxide nanosheets (FeOOH) introduces a RC series subcircuit that governs the hysteresis behavior; Si/Ge doubled layered nanotube anodes (Si/Ge DLNT) in which the Ge shell plays a role as an electron supplier; and carbon-coated zinc ferrite anodes ($\text{ZnFe}_2\text{O}_4\text{-C}$) where impedance study allows for the quantification of the kinetic parameters governing the various lithiation steps. For the first two types of anodes the equivalent circuit shown in Fig. 1f is employed, whereas in the case of $\text{ZnFe}_2\text{O}_4\text{-C}$ anodes a new mechanism at high frequencies must be taken into account incorporating a new branch in the proposed equivalent circuit, as it is explained below.

Amorphous FeOOH anodes present a highly porous nanostructure and a high surface area ($223 \text{ m}^2 \text{ g}^{-1}$).²⁴ In the first discharge, it is observed in Fig. 7a that at 0.95 V the specific capacity is 437 mA h g^{-1} , which corresponds to incorporation

of approximately 1.45 mol of Li per mol of FeOOH . The specific capacity of 914 mA h g^{-1} corresponds to the insertion of approximately 3 mol of Li per mol of FeOOH at a discharge potential of 0.5 V, implying complete conversion reaction between Li and FeOOH with the formation of elemental Fe and Li_2O ($\text{FeOOH} + 3\text{Li}^+ + 3\text{e}^- \rightarrow \text{Fe} + \text{Li}_2\text{O} + \text{LiOH}$). Electrodes also show good rate capability with a discharge capacity as high as 642 mA h g^{-1} at 1 C (Fig. 7b). EIS analysis of amorphous FeOOH electrodes at different states of discharge (SOD) and states of charge (SOC) has been studied after three charge-discharge cycles, once the conversion reaction is expected to be reversible and stabilized. This type of electrodes undergo an overall material rearrangement of both chemical and structural nature, leading us to regard the conversion reaction as the rate-limiting process of the change in electrode state of charge/discharge. The equivalent circuit in Fig. 1f allows for full analysis of the kinetic response.

The electrical parameters at different SOD and SOC have also been calculated from fitting in Fig. 8. The conversion reaction resistance $R_r \approx 500 \Omega$ is greater than R_{ct} , which implies that the conversion reaction limits the electrode charging. The conversion-reaction kinetics can be alternatively accessed by examining the response frequency. Values of ω_r (eqn (8)) below 0.04 s^{-1} are found.²⁴ Its maximum is located within the potential interval of the major conversion reaction according to the discharge voltage profile. Voltage shift in ω_r of $\sim 0.5 \text{ V}$ is noticed

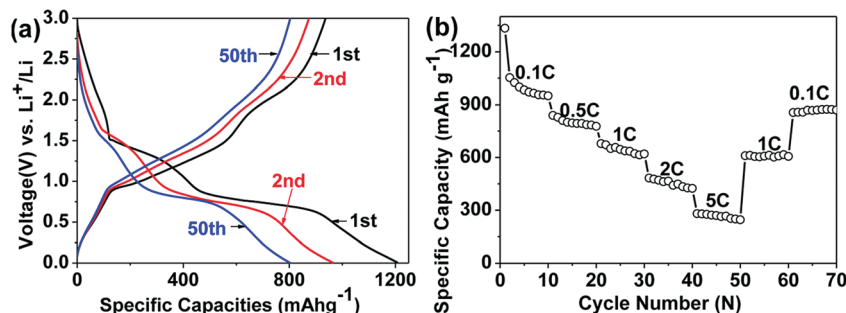


Fig. 7 (a) Charge–discharge voltage profiles of the 1st, 2nd and 50th cycle at a current density of 0.11 C (100 mA g⁻¹). (b) Cycling performance at different C rates. Reproduced (adapted) from ref. 24 with permission (2013) from American Chemical Society.

between discharge and charge regimes. This fact points to the hysteretic behavior of the conversion reaction.¹⁸ Therefore, EIS analysis reproduces the hysteresis observed between charge and discharge profiles in Fig. 7a. Accordingly, one can conclude that the conversion-reaction hysteresis has an origin related to the intrinsic thermodynamics rather than to transport limitations.²⁴

Another promising electrode candidate, alternative to carbon anodes in LIB, is Si because of its high specific theoretical capacity of 4200 mA h g⁻¹ when it is fully lithiated (Li₂₂Si₅). However, a considerable volumetric change, and then a fast capacity fading, is actually observed. For this reason, new materials are synthesized whose properties improve the cyclability, such as Si nanotubes (Si NTs) which exhibit a reversible morphology, but they are still limited by low electron conductivity and ionic diffusivity. On the other hand, the Si/Ge double-layered nanotube (Si/Ge DLNT) electrode shows improvements in structural stability and electrochemical kinetics. The Ge shell favors the incorporation of Li-ions from the electrolyte into the semiconductor structure, since Ge has higher electron conductivity than Si NTs and allows the charge transfer resistance associated to the incorporation of Li-ions to be reduced (Fig. 9).⁵¹ The kinetic limitations are explained by impedance methods using the equivalent circuit presented in Fig. 1e with additional RC series subcircuit accounting for external SEI films.

The kinetic limitations are easily associated with a resistive process that occurs during the test in a quasi-steady state. The Si NT electrodes present clearly an arc at intermediate frequencies associated with mechanisms that occur in a double layer formed by the nanotubes. R_{ct} increases in the Si NT when the potential falls below 0.5 V vs. Li/Li⁺ ($R_{ct} \approx 200 \Omega \text{ mg}$), while the incorporation of the Ge layer reduces this parameter to values as low as 3 $\Omega \text{ mg}$ (Fig. 10). Again changes in Li-ion intake suffice to explain differences in charging kinetics.

The conversion anode based on ZnFe₂O₄ exhibits a multi-step reaction process where intermediate phases of the Li–Zn–Fe–O system are formed as precursors of amorphous Li₂O. The full reaction involves a complete reduction of the metal and an additional alloy with Zn: ZnFe₂O₄ + 9Li⁺ + 9e⁻ → LiZn + 2Fe⁰ + 4Li₂O reaction, confirmed from a meticulous *in situ* XRD measurements determining the transition phases.⁵² Fig. 11 shows the main reactions taking place in lithiation–delithiation of the zinc ferrite nanoparticles. Zinc ferrite electrodes have a

high specific capacity and through a coating of carbon nanoparticles it is possible to maintain a fairly good kinetic performance in the high rate charge/discharge response. At lower charge states, the cell voltage decreases abruptly, related to the formation of the interfaces, kinetically and energetically favored. At potentials below 0.5 V an increment in the specific capacity appears as a tail with respect to the conversion-related plateau.²⁵

As commented upon previously, the electrodes involve a reorganization of the material of chemical and structural nature, that allows us to consider it as limiting the conversion reaction itself. The whole equivalent circuit to be used for electrode characterization is depicted in Fig. 1e. Here two reaction subcircuits are included accounting for the multistep lithiation mechanisms, which gives rise to two separate capacitive processes. The chemical capacitance exhibits then two contributions: C_{μ}^c corresponding to the full conversion reaction at lower potentials, and C_{μ}^i produced by intermediate lithiation Li–Zn–Fe–O phases (Fig. 12). At a lower potential, intermediate lithiation is masked by the huge C_{μ}^c values exhibited by the conversion process. In both cases, a rather monotonic increment occurs toward lower potentials with $C_{\mu}^c > C_{\mu}^i$ at a given charging state. It is interesting to compare here the capacitance extracted from EIS with the discharge curve derivative $-dQ/dV$ in Fig. 12a.

Fig. 12a allows inferring that while the discharge curve derivative is reduced at potentials below the peak at 1.0 V (which corresponds to the voltage plateau), the chemical capacitance exhibits higher values. This discrepancy can be understood by considering that the discharge curve at 40 mA g⁻¹ (C/20 rate) is still far from equilibrium conditions where EIS has been measured. This would entail that the discharge curve plateau prolongs in the case of ultraslow rates giving as a consequence increasing capacitances toward lower potentials.

Li–O₂ impedance response

To enhance the energy density storage in LIB technology, it is required to advance beyond the Li⁺ intercalation mechanisms. For Li–O₂ cathodes, the energy is stored by the direct reaction between Li⁺ ions and O₂ in a porous electrode that acts as an electric conductive substrate. This change in the chemistry of energy storage in the electrode is reflected in the EIS

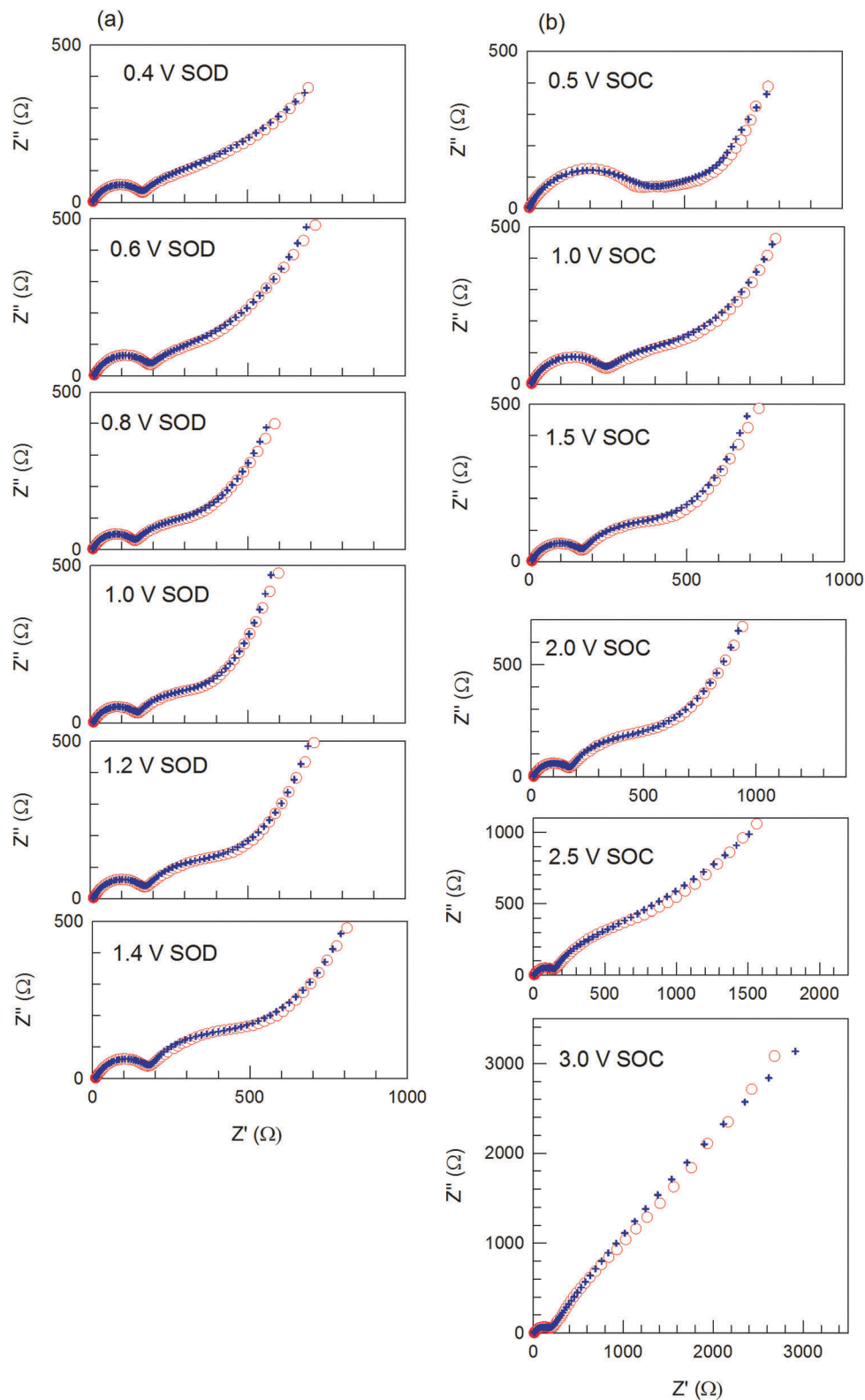


Fig. 8 Impedance response of amorphous FeOOH anodes measured at different voltages corresponding to either (a) discharge regime SOD or (b) charge regime SOC. Experimental data (dot) and fits (cross) are displayed for comparison. Reproduced (adapted) from ref. 24 with permission (2013) from American Chemical Society.

measurements which require different equivalent circuit models than those reported in previous sections.

Previous impedance analyses addressed the role of Li_2O_2 formation comparing the response of pristine and discharged electrodes.

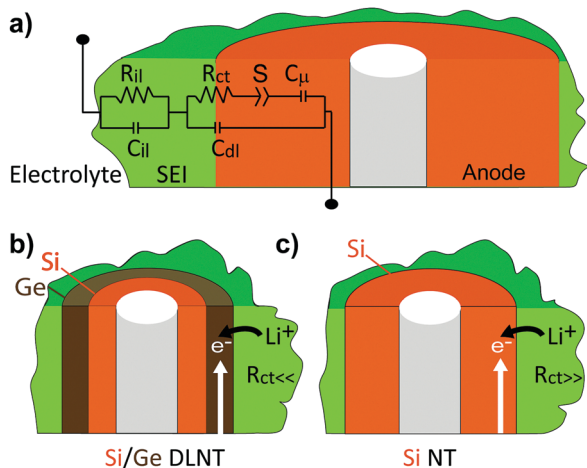


Fig. 9 Schematic view of the relationship between equivalent circuit elements and the electrode layer in Si/Ge and Si NT electrodes. In the equivalent circuit, the S element accounts for the reaction-assimilated resistance R_r , as represented in Fig. 1e. The solid state interface is commonly formed after cycling and introduces additional RC subcircuits. Reproduced (adapted) from ref. 51 with permission from Royal Society of Chemistry.

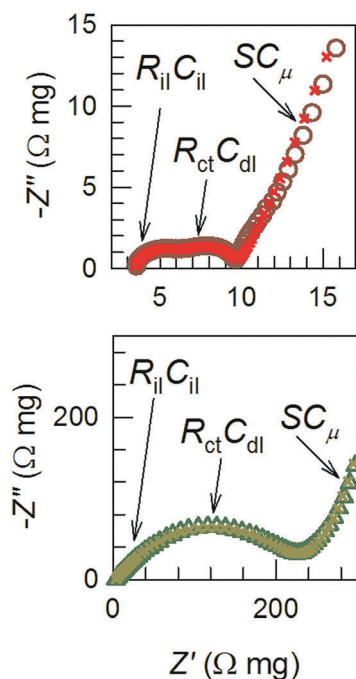


Fig. 10 Impedance spectroscopy response of Si/Ge DLNT (circle) and Si NT (triangle) electrodes at 0.1 V. Reproduced (adapted) from ref. 51 with permission from Royal Society of Chemistry.

Huang *et al.*³⁴ observed how the impedance evolves and signals the locus for ORR from the original electrode–electrolyte interface to the newly emerging Li_2O_2 –electrolyte interface. This last interface favors the ORR (through the reduction of the charge transfer resistance and activation energy), but introduces an impediment for electronic transport in the insulating Li_2O_2 layer. Also Rojo and co-workers proposed a complete equivalent circuit accounting for both ORR and OER involving the

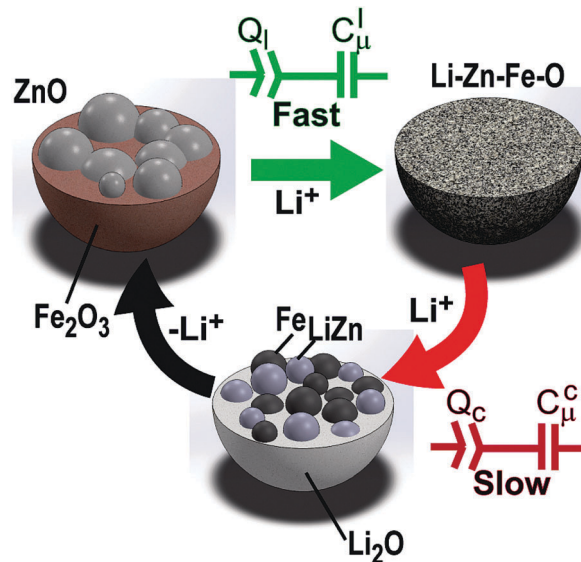


Fig. 11 Schematic representation of the main process occurring in the carbon coated $\text{ZnFe}_2\text{O}_4\text{-C}$ nanoparticle. Fast and slow charging sub-circuits are drawn in connection with the involved reactions. Q elements account for the reaction-assimilated resistance R_r , as represented in Fig. 1e. Reproduced (adapted) from ref. 25 with permission (2014) from American Chemical Society.

formation of Li_2O_2 and Li_2CO_3 discharge subproducts.⁵³ Højberg *et al.*⁵⁴ investigated by EIS the origin of the large overpotential usually observed between discharge and charge curves. Impedance measurements show that the increase in charge potential is not caused by larger internal resistances, but dictated by a mixed potential of parasitic reactions and Li_2O_2 oxidation. Even measuring the capacitance at a given frequency has been used to monitor the state of charge of the battery.⁵⁵ In any way, the detailed analysis of the extended C_{dl} can be a useful tool to evaluate the mechanism of cathode performance loss: clog of the porosity or coverage of the electric conductive substrate by the electrically insulating products (Li_2O_2 and Li_2CO_3) as reported in other studies.⁵⁶ The main differences between our equivalent circuit model and others proposed in the literature for Li– O_2 batteries are two: the identification of the extended double-layer capacitance related to the Li^+ adsorption and the observation of the ORR related phenomena only at voltages and frequencies below 2.7 V and 10 mHz.

To elucidate the equivalent circuit model, EIS measurements were carried out in different cathodes during the discharge process in the presence (with) and absence (w/o) of O_2 .⁵⁷ Fig. 13a shows two representations of these measurements: the impedance plot obtained at 2.6 V and the capacitance spectra $C = 1/i\omega Z$, versus the characteristic time (inverse of measuring frequency) in which the capacitive steps during the discharge process are represented by plateaus. In the absence of O_2 , the same impedance plot is registered in all the voltage range (between 4.2 and 2.2 V), with an arc above 5 Hz related to a first plateau (blue square in Fig. 13b), and a capacitive response below 5 Hz with the observation of a second plateau (orange square in Fig. 13b). In the presence of O_2 , a similar response to

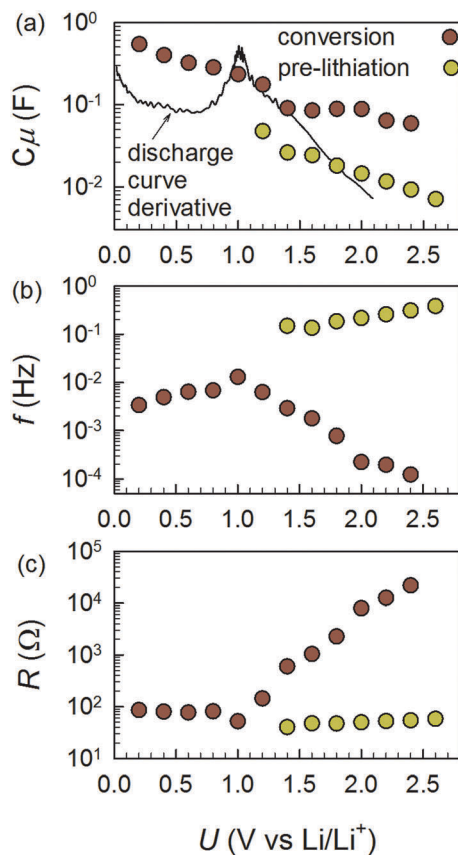


Fig. 12 Fitting results using the equivalent circuit of Fig. 1e showing (a) chemical capacitance C_μ , (b) reaction frequency $f = \omega_r/2\pi$, and (c) reaction equivalent resistance R_r , for the prelithiation Li–Zn–Fe–O phases formation, and the main conversion-alloying mechanism. In (a) the solid line corresponds to the derivative of the discharge curve $-dQ/dV$. Reproduced (adapted) from ref. 25 with permission (2014) from American Chemical Society.

that described for the absence of O_2 is obtained at voltages above the O_2 adsorption reaction ($\text{O}_2 + e^- \leftrightarrow \text{O}_2^-$, $E^0 = 2.71$ V). However, the impedance plot changes drastically at 2.6 V, with the presence of a third arc between 5 Hz and 10 mHz, and followed by a diffusion tail. The capacity response (Fig. 13b) also changes with the decrease of 1 order of magnitude of capacity in the second plateau followed by a steep increase.

With these data, we proposed an equivalent circuit model (Fig. 13c) in which the electrode discharge develops in three processes: (i) interfacial phenomena ($f > 5$ Hz) that are O_2 dependent. In the presence of O_2 (Fig. 13a), the impedance plot shows an extra arc ascribed to the solid film formed on the cathode containing Li_2O_2 and Li_2CO_3 , products in the reaction between Li ions and O_2 . (ii) Electrical double layer capacitance, EDLC (10 mHz $< f < 5$ Hz), that is O_2 independent at voltages above the O_2 adsorption reaction. This process is related to ion transport along the tortuous path of the porosity of the carbon matrix with concomitant surface accumulation.⁵⁸ The decrease of almost one order of the extended C_{dl} indicates that the adsorption of O_2 displaces the previously adsorbed Li^+ ions in a kinetic competition between Li^+ adsorption and consumption by oxygen reduction reaction (ORR). It provides information of

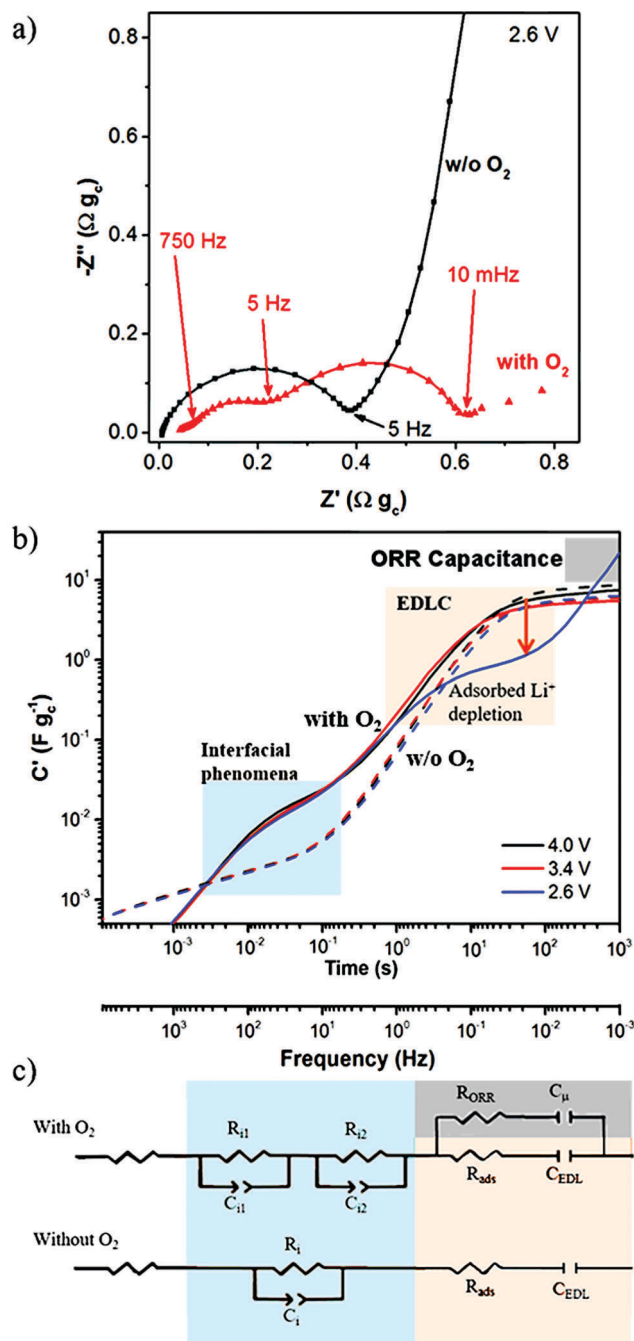


Fig. 13 (a) Impedance plot at 2.6 V vs. Li^+/Li , and (b) capacitance vs. characteristic time and frequency (in the opposite order than usual, from fast to slow electrochemical processes for a more intuitive reading) for a carbon electrode in the presence (solid lines) and absence (dashed lines) of O_2 . (c) Equivalent circuit model for the system in the absence and presence of O_2 . Reproduced (adapted) from ref. 57 with permission from Wiley-VCH.

the state of carbon surface.⁵⁷ (iii) Chemical ORR capacitance ($f < 10$ mHz) that only appears in the presence of O_2 . The equivalent circuit model (Fig. 13c) shows a new parallel branch to the extended C_{dl} subcircuit when O_2 starts to react (below 2.7 V), containing the chemical capacitance, C_μ , in series to the associated resistance, R_{ORR} , accounting for the reduction reaction.

Actually, more elements are needed related to the O₂ diffusion through different layers, since the real part of the impedance (Z') increases in the tail below 10 mHz, but very slow measurements should be required for a more concise model.

Conclusions

This Feature Article presents a survey on the applicability of recently proposed equivalent circuit models to the analysis of the lithiation kinetics of several kinds of battery electrodes. These new models appear as a consequence of observing electrode mechanisms by means of standard electrochemical impedance spectroscopy. As explained previously, kinetic limitation to the charging process has been mainly understood in terms of hindrances to ionic or electronic transport. Here a survey of impedance analysis of kinetic limitations to the electrode reduction is connected to the concept of reaction-limited charging. The low-frequency part of the impedance spectra conveys useful information about reaction limitations. For some oxides such as LiFePO₄, Li[Ni_{0.80}Co_{0.06}Mn_{0.14}]O₂, and TiO₂ the newly proposed models have been proved to be useful for identification of the mechanism. The model is fully exploitable in the case of conversion and alloying electrodes for which a complete rearrangement of the material structure is expected. Here, several electrode materials with different morphologies (FeOOH, ZnFe₂O₄ and Si/Ge) have been summarized. In many cases, improvement in electrode rate capability correlates with the reduction in charge-transfer resistance favored by electronic contacting strategies. For the sake of completeness, the special instance of Li–O₂ electrodes is also included to present the great potential of impedance analysis for the analysis of electrical mechanisms, at interfaces as well as at the particle bulk, in electrode materials.

Conflicts of interest

There are no conflicts to declare.

Acknowledgements

The authors acknowledge fruitful discussions with Prof. Bisquert and Prof. Passerini. We acknowledge Generalitat Valenciana for financial support under Project (PROMETEO/2014/020) and Ministerio de Economía y Competitividad (MINECO) of Spain under Project (MAT2016-76892-C3-1-R). N. V. acknowledges Universitat Jaume I for the support through FPI Fellowship Program (PREDOC/2015/54) and Project (UJI-B2016-35). The SCIC of Universitat Jaume I is also acknowledged.

References

- 1 D. D. Macdonald, *Electrochim. Acta*, 2006, **51**, 1376–1388.
- 2 M. E. Orazem and B. Tribollet, *Electrochemical Impedance Spectroscopy*, John Wiley & Sons, Hoboken, New Jersey, 2008.
- 3 B.-Y. Chang and S.-M. Park, *Annu. Rev. Anal. Chem.*, 2010, **3**, 207–229.
- 4 A. Lasia, *Electrochemical Impedance Spectroscopy and its Applications*, Springer, New York, 2014.
- 5 T. Hang, D. Mukoyama, H. Nara, N. Takami, T. Momma and T. Osaka, *J. Power Sources*, 2013, **222**, 442–447.
- 6 Y.-S. Su and A. Manthiram, *Nat. Commun.*, 2012, **3**, 1166.
- 7 S. H. Ng, J. Wang, Z. P. Guo, J. Chen, G. X. Wang and H. K. Liu, *Electrochim. Acta*, 2005, **51**, 23–28.
- 8 M. Itagaki, N. Kobari, S. Yotsuda, K. Watanabe, S. Kinoshita and M. Ue, *J. Power Sources*, 2005, **148**, 78–84.
- 9 *Impedance Spectroscopy: Theory, Experiment, and Applications*, ed. E. Barsoukov and J. R. Macdonald, John Wiley & Sons, Hoboken, New Jersey, 2005.
- 10 J. Song and M. Z. Bazant, *J. Electrochem. Soc.*, 2013, **160**, A15–A24.
- 11 A. Eftekhari, *ACS Sustainable Chem. Eng.*, 2017, **5**, 2799–2816.
- 12 *Nanomaterials for Lithium-Ion Batteries: Fundamentals and Applications*, ed. R. Yazami, CRC Press, Boca Raton, Florida, 2013.
- 13 J. Bisquert, *Nanostructured Energy Devices: Equilibrium Concepts and Kinetics*, CRC Press, Boca Raton, FL, 2015.
- 14 T. Pajkossy and R. Jurczakowski, *Current Opinion in Electrochemistry*, 2017, **1**, 53–58.
- 15 J. Jamnik and J. Maier, *Phys. Chem. Chem. Phys.*, 2001, **3**, 1668–1678.
- 16 J. Bisquert, *J. Phys. Chem. Phys.*, 2003, **5**, 5360–5364.
- 17 J. Bisquert, G. Garcia-Belmonte, F. Fabregat-Santiago and P. R. Bueno, *J. Electroanal. Chem.*, 1999, **475**, 152–163.
- 18 J. Cabana, L. Monconduit, D. Larcher and M. R. Palacin, *Adv. Mater.*, 2010, **22**, E170–E192.
- 19 J. E. B. Randles, *Discuss. Faraday Soc.*, 1947, **1**, 11–19.
- 20 J. Bisquert and A. Compte, *J. Electroanal. Chem.*, 2001, **499**, 112–120.
- 21 G. Garcia-Belmonte, Z. Pomerantz, J. Bisquert, J.-P. Lellouche and A. Zaban, *Electrochim. Acta*, 2004, **49**, 3413–3417.
- 22 J. García-Cañadas, F. Fabregat-Santiago, I. Porqueras, C. Person, J. Bisquert and G. Garcia-Belmonte, *Solid State Ionics*, 2004, **175**, 521–525.
- 23 J. Bisquert, G. Garcia-Belmonte and A. Pitarch, *ChemPhysChem*, 2003, **4**, 287–292.
- 24 C. Xu, Y. Zeng, X. Rui, J. Zhu, H. Tan, A. Guerrero, J. Toribio, J. Bisquert, G. Garcia-Belmonte and Q. Yan, *J. Phys. Chem. C*, 2013, **117**, 17462–17469.
- 25 F. Martinez-Julian, A. Guerrero, M. Haro, J. Bisquert, D. Bresser, E. Paillard, S. Passerini and G. Garcia-Belmonte, *J. Phys. Chem. C*, 2014, **118**, 6069–6076.
- 26 M. D. Levi and D. Aurbach, *J. Phys. Chem. B*, 2004, **108**, 11693–11703.
- 27 J. P. Meyers, M. Doyle, R. M. Darling and J. Newman, *J. Electrochem. Soc.*, 2000, **147**, 2930–2940.
- 28 J. Bisquert, G. Garcia-Belmonte, F. Fabregat-Santiago and A. Compte, *Electrochem. Commun.*, 1999, **1**, 429–435.
- 29 C. Wang, A. J. Appleby and F. E. Little, *Electrochim. Acta*, 2001, **46**, 1793–1813.
- 30 Q.-C. Zhuang, X.-Y. Qiu, S.-D. Xu, Y.-H. Qiang and S.-G. Sun, in *Lithium Ion Batteries – New Developments*, ed. I. Belharouak, In Tech, Rijeka, 2012.
- 31 Q.-C. Zhuang, T. Wei, L.-L. Du, Y.-L. Cui, L. Fang and S.-G. Sun, *J. Phys. Chem. C*, 2010, **114**, 8614–8621.
- 32 J. Bisquert and V. S. Vikhrenko, *Electrochim. Acta*, 2002, **47**, 3977–3988.
- 33 T. M. Bandhauer, S. Garimella and T. F. Fuller, *J. Electrochem. Soc.*, 2011, **158**, R1–R25.
- 34 J. Huang and B. Tong, *Chem. Commun.*, 2017, **53**, 11418.
- 35 S. S. Zhang, K. Xu and T. R. Jow, *Electrochim. Acta*, 2004, **49**, 1057–1061.
- 36 T. Momma, M. Matsunaga, D. Mukoyama and T. Osaka, *J. Power Sources*, 2012, **216**, 304–307.
- 37 Z. Deng, Z. Zhang, Y. Lai, J. Liu, J. Li and Y. Liu, *J. Electrochem. Soc.*, 2013, **160**, A553–A558.
- 38 U. Troltzsch, O. Kanoun and H.-R. Trankler, *Electrochim. Acta*, 2006, **51**, 1664–1672.
- 39 K.-J. Park, B.-B. Lim, M.-H. Choi, H.-G. Jung, Y.-K. Sun, M. Haro, N. Vicente, J. Bisquert and G. Garcia-Belmonte, *J. Mater. Chem. A*, 2015, **3**, 22183–22190.
- 40 N. Vicente, M. Haro, D. Cíntora-Juárez, C. Pérez-Vicente, J. L. Tirado, S. Ahmad and G. Garcia-Belmonte, *Electrochim. Acta*, 2015, **163**, 323–329.
- 41 *Lithium Batteries: Science and Technology*, ed. G.-A. Nazri and G. Pistoia, Springer Science + Business Media, New York, 2009.
- 42 S. Martha, E. Markevich, V. Burgel, G. Salitra, E. Zinigrad, B. Markovskiy, H. Sclar, Z. Pramovich, O. Heik and D. Aurbach, *J. Power Sources*, 2009, **189**, 288–296.

- 43 H.-J. Noh, S. Youn, C. S. Yoon and Y.-K. Sun, *J. Power Sources*, 2013, **233**, 121–130.
- 44 B. Hwang, Y. Tsai, D. Carlier and G. Ceder, *Chem. Mater.*, 2003, **15**, 3676–3682.
- 45 A. K. Padhi, K. Nanjundaswamy and J. B. Goodenough, *J. Electrochem. Soc.*, 1997, **144**, 1188–1194.
- 46 G. Li and P. G. Pickup, *Phys. Chem. Chem. Phys.*, 2000, **2**, 1255–1260.
- 47 P. Acevedo-Peña, M. Haro, M. E. Rincón, J. Bisquert and G. Garcia-Belmonte, *J. Power Sources*, 2014, **268**, 397–403.
- 48 R. Hass, J. Garcia-Cañadas and G. Garcia-Belmonte, *J. Electroanal. Chem.*, 2005, **577**, 99–105.
- 49 N. Vicente and G. Garcia-Belmonte, *J. Phys. Chem. Lett.*, 2017, **8**, 1371–1374.
- 50 N. Vicente and G. Garcia-Belmonte, *Adv. Energy Mater.*, 2017, **7**, 1700710.
- 51 M. Haro, T. Song, A. Guerrero, L. Bertoluzzi, J. Bisquert, U. Paik and G. Garcia-Belmonte, *Phys. Chem. Chem. Phys.*, 2014, **16**, 17930.
- 52 D. Bresser, E. Paillard, R. Kloepsch, S. Krueger, M. Fiedler, R. Schmitz, D. Baitner, M. Winter and S. Passerini, *Adv. Energy Mater.*, 2013, **3**, 513–523.
- 53 I. Landa-Medrano, I. R. de Larramendi, N. Ortiz-Vitoriano, R. Pinedo, J. I. R. de Larramendi and T. Rojo, *J. Power Sources*, 2014, **249**, 110–117.
- 54 J. Højberg, B. D. McCloskey, J. Hjelm, T. Vegge, K. Johansen, P. Norby and A. C. Luntz, *ACS Appl. Mater. Interfaces*, 2015, **7**, 4039–4047.
- 55 A. E. Christensen, J. Højberg, P. Norby and T. Vegge, *J. Electrochem. Soc.*, 2015, **162**, A2075–A2079.
- 56 B. D. McCloskey, A. Speidel, R. Scheffler, D. C. Miller, V. Viswanathan, J. S. Hummelshøj, J. K. Nørskov and A. C. Luntz, *J. Phys. Chem. Lett.*, 2012, **3**, 997–1001.
- 57 M. Haro, N. Vicente and G. Garcia-Belmonte, *Adv. Mater. Interfaces*, 2015, **2**, 1500369.
- 58 G. Rasines, P. Lavela, C. Macías, M. Haro, C. Ania and J. Tirado, *J. Electroanal. Chem.*, 2012, **671**, 92–98.